Compression Freezing Kinetics of Water to Ice VII

A. E. Gleason,[1,2,*] C. A. Bolme,[1] E. Galtier,[3] H. J. Lee,[3] E. Granados,[3] D. H. Dolan,[4] C. T. Seagle,[4] T. Ao,[4] S. Ali,[5] A. Lazicki,[5] D. Swift,[5] P. Celliers,[5] and W. L. Mao[2,6]

[1]*Shock and Detonation Physics, Los Alamos National Laboratory, Los Alamos, New Mexico 87545 USA*
[2]*Stanford Institute for Materials and Energy Sciences, SLAC National Accelerator Laboratory, Menlo Park, California 94025 USA*
[3]*Linac Coherent Light Source, SLAC National Accelerator Laboratory, Menlo Park, California 94025 USA*
[4]*Sandia National Laboratories, Albuquerque, New Mexico 87185 USA*
[5]*Shock Physics, Lawrence Livermore National Laboratory, Livermore, California 94550 USA*
[6]*Geological Sciences, Stanford University, Stanford, California 94305 USA*

(Received 24 March 2017; revised manuscript received 22 May 2017; published 11 July 2017)

Time-resolved x-ray diffraction (XRD) of compressed liquid water shows transformation to ice VII in 6 nsec, revealing crystallization rather than amorphous solidification during compression freezing. Application of classical nucleation theory indicates heterogeneous nucleation and one-dimensional (e.g., needlelike) growth. These first XRD data demonstrate rapid growth kinetics of ice VII with implications for fundamental physics of diffusion-mediated crystallization and thermodynamic modeling of collision or impact events on ice-rich planetary bodies.

DOI: 10.1103/PhysRevLett.119.025701

Background.—Understanding the phase diagram and properties of H_2O, a ubiquitous molecule in the Universe and primary building block of icy satellites and water-rich exoplanets, is crucial for physics and planetary science and has motivated studies on water under extreme conditions for nearly a century [1]. It possesses a complicated high-pressure (P),–temperature (T) phase diagram where high pressure phases exhibit novel phenomena and intriguing properties, e.g., solid ice Ih having a lower density than liquid water, ice Ih with an anomalous Clausius-Clapeyron slope, low-T, high-P polyamorphism [2], and a superionic phase at ultrahigh pressure (e.g., Ref. [3]). Static- (e.g., Refs. [3–5]) and dynamic-compression (e.g., Refs. [6–8]) experiments have been used to generate high-P and/or–T conditions from which to study the complex H_2O phase diagram, chemical properties, and kinetics. Dynamic experimental platforms combined with optical transmission and imaging provide insights into changes in state and phase at short time scales [6,9]. In particular, quasi-isentropic dynamic compression, via reverberation (multiple shock loading) or ramp-wave propagation, has been used to achieve high pressure states at lower temperatures, allowing access to phases below the H_2O melt boundary, such that the entropy is only slightly increased due to plastic work heating or viscosity. Dolan *et al.* [10] observed liquid water to undergo a first order phase transition using quasi-isentropic compression to a solid in less than 10 nsec, but did not have combined temporal and spatial resolution to extract information about the resultant high-pressure phase and transformation mechanism. Similarly, Bastea *et al.* [11] explored the kinetics of overcompressed water transforming to a solid using velocimetry measurements combined with hydrocode simulations, finding the resultant high-pressure phase properties most like ice VII. The fast mechanical loading of shock waves as a dynamic compression tool combined with ultrafast x-ray probes provide unique access to material-based time scales revealing rapid disorder-to-order transitions in condensed matter [12]. Here, with femtosecond XRD, we provide an upper bound on the time scale for compression-based freezing of water and establish heterogeneous nucleation of body-centered-cubic crystalline structure, ice VII, at extreme conditions.

Results.—Atomic structure measurements of quasi-isentropically compressed (see Fig. 1 of the Supplemental Material [13]) water were made using transmission *in situ* XRD with 7.6 keV x rays from the x-ray free electron laser (XFEL) at the matter in extreme conditions (MEC) end station of the Linac Coherent Light Source (LCLS) (Fig. 1). This ramp-style compression is achieved through temporally tailoring a drive laser that slowly increases ablation energy over 15 ns. The target geometry consisted of a clamp-style water containment approach [29]. Individual packages of sandwiched diamond—water—quartz served as the target: [80 um thick ⟨110⟩ single-crystal diamond] + [155 um deionized water (18 MOhm) layer set by a circular silicone washer (Silastic J, Dow Corning)] + [40 um c-cut α quartz]. A 75 nm gold layer served as the reflective layer for velocimetry and as an internal pressure calibrant.

XRD from each pump-probe experiment, recorded on the Cornell-SLAC Pixel Array Detectors (CSPADs), is azimuthally integrated (Fig. 2) as a function of x-ray scattering angle (2θ) (see Methods). Ambient condition XRD patterns record the diffuse scatter from the liquid water (between ~30–53°2θ) plus three gold peaks. XRD measurements are spatially integrated through the whole sample, and therefore the diffraction measures varying

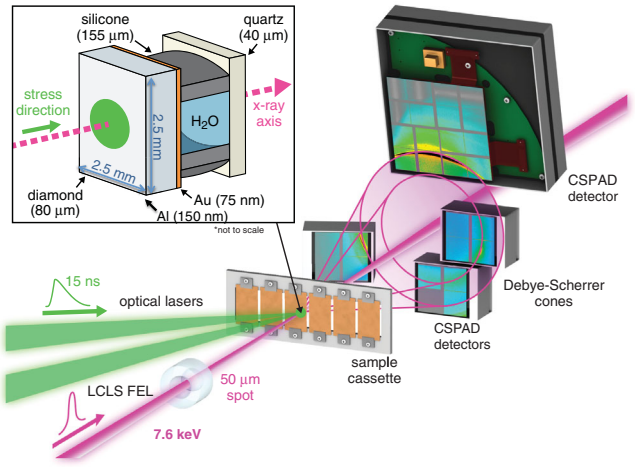

FIG. 1. Experimental configuration of the XFEL probe and optical laser. The shock freezing behavior of water captured in a Debye-Scherrer geometry. *Inset:* Schematic of target package as a cut away side view.

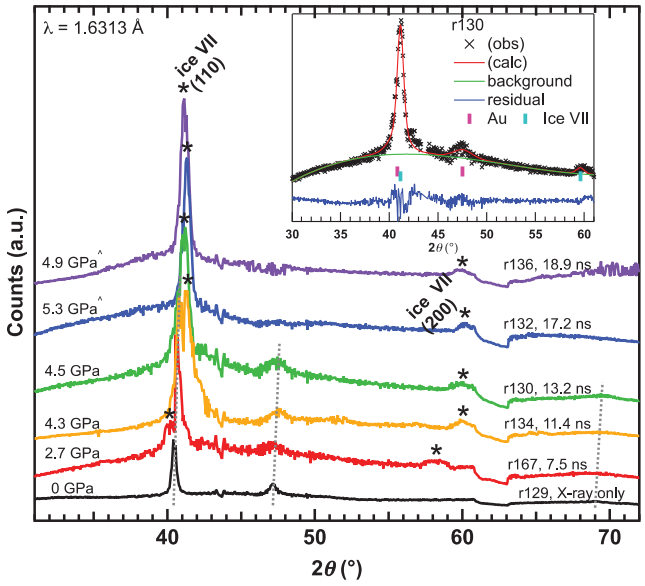

FIG. 2. Multiplot of time-resolved x-ray diffraction data. Dark subtracted raw diffraction data plotted without any additional normalization. Traces are offset for visual clarity. Ice VII (110) and (200) peaks are marked with asterisks. Au (111), (200), and (220) peak position trends are marked with dashed grey lines. Au is used to estimate pressure for traces between 7.5–13.2 ns (Refs. [32,33]). Samples for the last two traces, 17.2 and 18.9 ns, did not have a Au coating; therefore, pressures (denoted with ˆ) are estimate from the ice VII equation of state [5]. Breaks in the detector are seen at 2θ of 43.5°, 49.5°, and 61°. *Inset:* Example of Rietveld refinement performed on run 130 showing good agreement between the observed and calculated patterns.

contributions from ambient and compressed target package materials as a function of time due to the ramp-wave propagation. A relative time zero is defined as the time when the ramp wave enters the water. As the wave propagates through the water, time-delayed diffraction, from 7.5 to 18.9 ns, shows compression of the gold and emergence of two new peaks at ~40° and ~58°2θ. These peaks shift to slightly higher 2θ as the compression wave transits the sample and pressure increases. The new peaks are indexed as high-pressure crystalline ice VII (body-centered cubic, *P*n-3m used in the second origin setting in GSAS) [30]. The relative intensities of the first two Bragg reflections (110) and (200) show no preferred orientation (i.e., comparable relative intensities to Refs. [5,31]). Rietveld refinement is a powerful tool for quantitative crystal structure analysis, widely used in the x-ray diffraction community. Our Rietveld refinement parameters and example profile fit pattern are listed in the Supplemental Material Table 1 and Fig. 2 inset, respectively. Pressures are derived from the peak positions of internal Au calibrant. These pressures include a small (few percent) thermal correction due to heating from quasi-isentropic compression [32,33]. We find excellent agreement between the temperature corrected ice VII unit cell volume derived pressure and the internal Au calibrant (Supplemental Material Table 1), recording *P*, *T* conditions of ~2 GPa, 350 K to ~5 GPa, 400 K, Ref. [5]. The last two time-resolved traces, runs 132 and 136, did not contain gold; therefore, we estimate pressure using the ice VII unit cell volume. Our peak positions do not match hexagonal ice VI, a candidate high pressure ice phase previously observed at ~2 GPa, 350 K in static compression experiments [5]. Recent computational work suggests rapid freezing of liquid water to a plastic ice phase with the same translational order as ice VII, with the molecules rotating freely [34]. Our 2θ coverage and peak intensity ratios do not allow us to distinguish between crystalline ice VII and plastic ice.

Velocimetry data, recorded on the velocity interferometer system for any reflector (VISAR) system, used the Au reflective surface and were collected simultaneously with XRD (example run 130, Fig. 3); analysis given in Supplemental Materials, Discussion 1 [13]. Because of shot-to-shot variation in VISAR quality and (possible) issues of field-of-view alignment vs x-ray probe, we use the velocimetry data only in the capacity to compliment diffraction interpretation and not to strictly constrain pressures. Indication of a velocity "push forward" at 3 ns or 6 ns (Fig. 3) corroborates the onset of a phase transition to high pressure crystalline phase, resolvable in the XRD by 7.5 ns. Moreover, VISAR measurements confirm the sample is not directly shocking from an ambient to peak state—providing evidence that the temperatures are low enough to form ice VII.

Individual liquid cell targets suited for high-repetition rate laser shock are technically challenging to design and fabricate. The clamp-style sealing mechanism induces a level of contamination of the deionized water by the gasketing material, in this case, silicone. Preshot fresh water filtration is not possible, and a water sample is in contact with silicone for 6–12 h preceding the shot. We

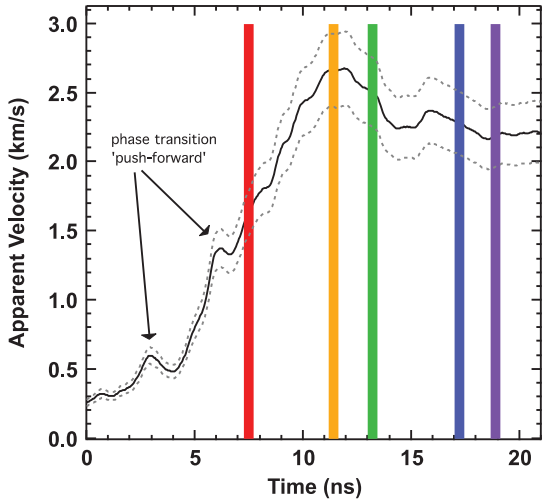

FIG. 3. VISAR spatially averaged lineout. An average of the central 100 μm region of the apparent velocity histories. Colored bars (matched to Fig. 2 traces) indicate XFEL probe time where width of the bar includes the $+/-350$ ps timing uncertainty.

quantified the Si contamination by radial diffusion from the silicone into deionized water using ICP-MS (see Supplemental Methods, Discussion 2 [13]), finding the aqueous Si-species concentration to be, at most, a few ppm.

Discussion.—According to classical nucleation theory (e.g., Ref. [35]), the descriptions of homogeneous and heterogeneous nucleation are similar. The transformation kinetics are described by a rate equation, commonly referred to as the Johnson-Mehl-Avrami-Kolmogorov (JMAK) model [36–38] for the transformed mass or volume fraction with an exponential functional form,

$$\alpha(t) = 1 - \exp(-(k(t-\tau))^n, \quad (1)$$

where $\alpha(t)$ is the fraction of the material transformed as a function of time, t, k is a crystallization rate constant, τ is incubation time, and n is the JMAK kinetic exponent. The kinetic exponent contains contributions from nucleation probability and growth topology. JMAK theory is traditionally applied to ambient pressure melt quench experiments to extract details about the transformation mechanism, generally assuming a random distribution of nucleation sites [39]. However, due to the destructive nature of a dynamic-compression experiment, quantification of *in situ* phase transformed volume fractions has not been possible until now. Using our time-resolved XRD of ice VII and phase fraction analysis from Rietveld refinement, we examine the crystallization kinetics of H_2O, providing insights for the basic mechanism of the transition during isentropic compression [Fig. 4(a)]. The mass fraction of ice VII as a function of time [Fig. 4(b)] for 7–13 ns is determined using the internal phase fraction marker method, e.g., Au layer, (Supplemental Methods, Discussion 3 [13]), whereas the later two time slices (17–19 ns) do not have an Au layer. These phase fractions were assessed using the sum of areas under Gaussian fits to ice VII (110) and (200) peaks relative to the total area under the trace with a twofold increase in the uncertainty relative to the internal marker method. The best-fit parameters for the JMAK model to our data are $\tau = 6.4(\pm 1.1)$ ns, $n = 0.6(\pm 0.2)$, and $k = 0.010(\pm 0.007)$ ns^{-1} [Fig. 4(b), red curve]. We investigate a range of parameter combinations for comparison of goodness of fit [Fig. 4(b), grey curves and Supplemental Method, Discussion 4 [13]]. An incubation time of $\tau = 6.4$ ns for crystallization to begin is representative of the first nucleation event(s) and fast for a disorder-to-order transition. Dolan and Gupta [7] extrapolate an incubation time of 7 ± 2 ns at 5 GPa which is in excellent agreement with this work. A JMAK kinetic exponent of 1 is typically the lower bound for heterogeneous nucleation corresponding to nucleation on surfaces of, in this case, Si impurities [40,41].

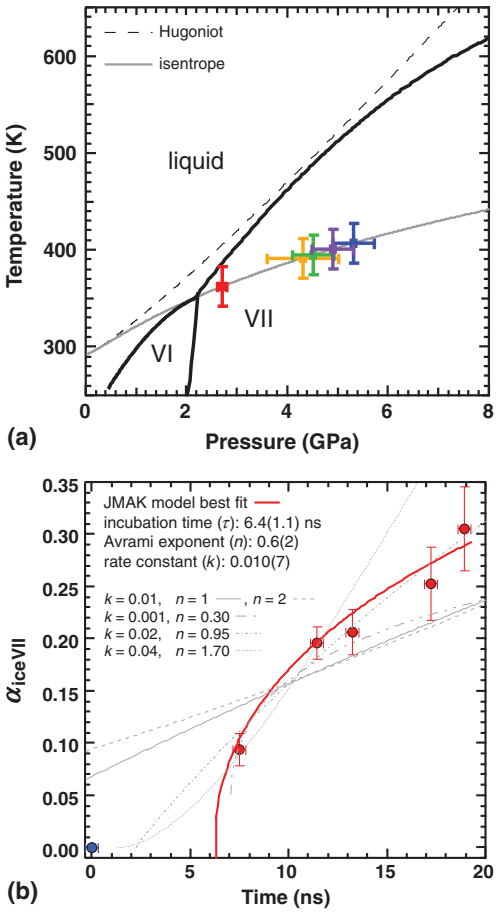

FIG. 4. Phase diagram of H_2O and trend in volume fraction converted to ice VII in explored phase space. (a) Equilibrium phase diagram of H_2O (Ref. [45]) and Hugoniot (dashed trace) and isentrope (grey trace) curves from IAPWS95 liquid equation of state [32]. Colored points show coverage of phase space accessed in this work with the (b) fraction converted to ice VII ($\alpha_{\mathrm{ice}VII}$, red points; blue point is starting time-zero fraction, not included in the fit). Best JMAK model fit (red curve) is compared to other combinations of JMAK parameters (grey curves).

Because of our impurity level, homogeneous would not be realistic since the presence of even trace amounts of Si would likely catalyze growth of small ice grains and lower the free energy barrier for crystallization. This finding is reinforced by Sun *et al.* [42] who demonstrate that the more inhomogeneous the distribution of nucleation sites, the lower the JMAK kinetic exponent—which could indicate our Si impurities are not uniformly disbursed. Therefore, our incubation time is an upper limit demonstrating how fast nucleation can proceed due to the presence of a spatially heterogeneous distribution of ppm impurities. More recently, $n \leq 1$ is thought to be indicative of diffusion-controlled crystallization and heterogeneous, likely simultaneous, nucleation [43]. This fast crystallization rate may support a one-dimensional grain growth geometry, as in needles or rods [43,44]. Admittedly, JMAK theory is phenomenological and may not be ideal for all dynamic compression data sets; yet in the absence of a more exact kinetics model available at this time, we rely on the JMAK basic functional form to give a qualitative, physical picture of transformation [39]. Moreover, this new experimental platform enables high-spatial and–temporal fidelity XRD from which phase fraction extraction can encourage the kinetics modeling community to make advancements.

Direct observations of ice VII formation under ramp compression have implications ranging from fundamental physics of diffusion-mediated primary crystallization to modeling of constituent planetary materials. In particular, we show that dynamic phase transformations can result in crystallization (also, e.g., Ref. [12]), not necessarily amorphization. In the context of ice phases present in icy moons and extrasolar planetary bodies, evaluation of extreme condition behavior of impurity-laden ices is critical for modeling of planetary interiors [46]. The mechanical and thermodynamic work from an impact event is typically derived from a material's shock Hugoniot describing dynamic strength and phase properties [47]—yet until now direct, lattice-level, time-resolved structural information approaching theoretical time scales was not available to validate optical transmission- or velocimetry-based measurements. Here, we see an almost immediate transformation to a high pressure ice slush (i.e., water-ice VII mixture). Compared to ice VII alone, this would effectively reduce the bulk modulus of the mixed phase system and lead to rapid loss of strength during the initial stages of an impact event. These new kinetics data could be used in modeling collisions onto and between ice-rich planets and cometesimals in the outer solar system and provide more information to understand the structure and petrology of their interiors.

Methods.—Quasimonochromatic ($dE/E = 0.2$–0.5%), fully transverse coherent, 7.603(30) keV x-ray pulses of 40 fs duration with an average of $\sim 10^{12}$ photons per pulse, were incident over a 50 μm diameter spot on the target package. An x ray only shot was collected before each drive shot as a reference. The 50 μm XFEL beam spot did not produce any observable x-ray damage to the target. Metal coatings on the diamond ablator served to absorb the drive laser (150 nm Al on upstream side) and act as the reflective layer for velocimetry measurements (75 nm Au on downstream side).

The optical drive laser was defocused to a 250 μm diameter spot at FWHM with a Gaussian spatial profile to achieve focal spot intensity of $\sim 10^{12}$ W/cm^2. The angle between drive laser arms and XFEL probe was 22°. An ablation-driven compression wave was launched parallel to the sample normal over a 15.0 ns ramp pulse profile (Supplemental Material Fig. 1 [13]) from a frequency doubled Nd:Glass laser system ($\lambda = 527$ nm). The optical laser and x-ray beam were spatially overlapped and operated in single shot mode. The absolute time zero corresponds to overlap of their leading edges. For each shot, a time delay was selected for the XFEL pulse relative to the optical laser pulse with a jitter of 0.35 ns. We establish a relative time zero defined as the time at which the pressure wave reaches the interface between the diamond and the water, where the transit time through the single crystal diamond is 4.40 (35) ns, Ref. [48]. The pump-probe delay scans at several nanosecond intervals enabled collection of a time series of XRD patterns in transmission geometry. XRD patterns were captured by Cornell-SLAC pixel array detectors (CSPADs) constructed of individual application-specific integrated circuits (ASICs) [49]. Maximum azimuthal angle coverage was 230°; however, because of the mosaic nature of the CSPADs, continuity of ice VII Debye rings was not possible over this range. Integrated data were collected over an 80° azimuthal range. One target was shot per time delay selected.

Using general structure analysis system (GSAS) software [30] with EXPGUI [50], we perform Rietveld refinements on all integrated diffraction data (starting crystallographic information file from Kamb and Davis [31]); an example is shown for run 130, inset of Fig. 2. Pixels associated with the spaces in between ASICs of the CSPADs have been removed for refinement. The goodness-of-fit factor (reduced χ^2) and lattice parameter (a) and unit cell volume (V) for each trace derived from each fit are listed in the Supplemental Materials Table 1 [13].

AEG and WLM are supported by the Geophysics Program at NSF (Grant No. EAR0738873) with additional support from LANL Reines LDRD for AEG and DOE-BES through SIMES for target fabrication costs. This work was performed at the Matter at Extreme Conditions (MEC) instrument of LCLS, supported by the U.S. DOE Office of Science, Fusion Energy Science under Contract No. SF00515, and was supported by LCLS, a National User Facility operated by Stanford University on behalf of the U.S. DOE, Office of Basic Energy Sciences. We thank LCLS/SLAC staff for assistance during the experiment, insightful discussions with S. Stewart, S. Bastea, and K. Weaver for the Stanford ICP-MS/TIMS Facility. Work of S. A., A. L., D. S., and P. C. was performed under the

auspices of the U.S. DOE by LLNL under Contract No. DE-AC52-07NA27344. Los Alamos National Laboratory is operated for the U.S. DOE National Nuclear Security Administration under Contract No. DE-AC52-06NA25396. Sandia National Laboratories is a multimission laboratory managed and operated by National Technology and Engineering Solutions of Sandia, LLC., a wholly owned subsidiary of Honeywell International, Inc., for the U.S. Department of Energy's National Nuclear Security Administration under Contract No. DE-NA0003525.

C. B. participated in the experiment and developed XRD projection software. E.Ga., H. J. L., and E.Gr. participated in the experiment as MEC instrument scientists and contributed to data interpretation. D. D., T. A., and C. S. contributed to interpretation and provided VISAR modeling/interpretation. W. M., S. A., A. L., D. S., and P. C. contributed to data collection. A. G. was principal investigator, analyzed the data, and wrote the paper.

The authors declare no competing financial interests.

*Corresponding Author.
arianna@lanl.gov

[1] P. Bridgeman, Proc. Am. Acad. Arts Sci. **74**, 399 (1942).
[2] O. Mishima and E. Stanley, Nature (London) **396**, 329 (1998).
[3] A. Goncharov, N. Goldman, L. E. Fried, J. C. Crowhurst, I.-F. W. Kuo, C. J. Mundy, and J. M. Zaug, Phys. Rev. Lett. **94**, 125508 (2005).
[4] R. Hemley, A. P. Jephcoat, H. K. Mao, C. S. Zha, L. W. Finger, and D. E. Cox, Nature (London) **330**, 737 (1987).
[5] L. Bezacier, B. Journaux, J.-P. Perrillat, H. Cardon, M. Hanfland, and I. Daniel, J. Chem. Phys. **141**, 104505 (2014).
[6] S. Kormer, K. Yushko, and G. Krishkevich, Sov. Phys. JETP **27**, 879 (1968).
[7] D. Dolan and Y. Gupta, J. Chem. Phys. **121**, 9050 (2004).
[8] S. Stewart and T. Ahrens, J. Geophys. Res. **110**, E03005 (2005).
[9] D. Dolan, J. Johnson, and Y. Gupta, J. Chem. Phys. **123**, 064702 (2005).
[10] D. Dolan, M. Knudson, C. Hall, and C. Deeney, Nat. Phys. **3**, 339 (2007).
[11] M. Bastea, S. Bastea, J. Reaugh, and D. Reis, Phys. Rev. B **75**, 172104 (2007).
[12] A. Gleason *et al.*, Nat. Commun. **6**, 8191 (2015).
[13] See Supplemental Material at http://link.aps.org/supplemental/10.1103/PhysRevLett.119.025701, which includes Refs. [14–28], for more details concerning drive profile, Lagrangian stress tracer plot, unit cell, and fit parameters for Rietveld refinements of Au and ice VII, and discussions of water sample purity, VISAR analysis, phase fraction assessment strategies, and JMAK model fit parameters.
[14] D. Bloomquist and S. Sheffield, J. Appl. Phys. **54**, 1717 (1983).
[15] P. Celliers, D. Bradley, G. Collins, D. Hicks, T. Boehly, and W. Armstrong, Rev. Sci. Instrum. **75**, 4916 (2004).
[16] T. Ao, Sandia Report No. SAND2009-3236, 2009.
[17] M. Takeda, J. Ina, and S. Kobayashi, J. Opt. Soc. Am. **72**, 156 (1982).
[18] W. Macy, Appl. Opt. **22**, 3898 (1983).
[19] D. Dolan, Ph.D. Thesis, Washington State University, 2003.
[20] H. Shimizu, T. Nabetani, T. Nishiba, and S. Sasaki, Phys. Rev. B **53**, 6107 (1996).
[21] M. Lang, F. X. Zhang, R. C. Ewing, J. Lian, C. Trautmann, and Z. Wang, J. Mater. Res. **24**, 1322 (2009).
[22] A. Gualtieri, A. Guagliardi, and A. Iseppi, *Diffraction Analysis of the Microstruct.ure of Materials.* (Springer-Verlag, Berlin, 2004).
[23] R. Snellings, L. Machiels, G. Mertens, and J. Elsen, Geologica Belgica **13**, 183 (2010).
[24] J. Malek, Thermochim. Acta **267**, 61 (1995).
[25] E. Dill, J. Folmer, and J. Martin, Chem. Mater. **25**, 3941 (2013).
[26] M. Bastea, S. Bastea, J. Reaugh, and D. Reisman, Phys. Rev. B **75**, 172104 (2007).
[27] D. Barahona, Atmos. Chem. Phys. **15**, 13819 (2015).
[28] M. Bastea, S. Bastea, and R. Becker, Appl. Phys. Lett. **95**, 241911 (2009).
[29] S. Ali, in *Gordon Research Conference, High Pressure Conf. Board 1-24* (ID 1281151, 2012).
[30] A. Larson and R. Von Dreele, Los Alamos National Laboratory Report No. LAUR 86–748 2000.
[31] B. Kamb and B. Davis, Proc. Natl. Acad. Sci. U.S.A. **52**, 1433 (1964).
[32] W. Wagner and A. Pruβ, J. Phys. Chem. Ref. Data **31**, 387 (2002).
[33] Y. Fei, A. Ricolleau, M. Frank, K. Mibe, G. Shen, and V. Prakapenka, Proc. Natl. Acad. Sci. U.S.A. **104**, 9182 (2007).
[34] J. Aragones and C. Vega, J. Chem. Phys. **130**, 244504 (2009).
[35] J. Christian, *The Theory of Transformations in Metals and Alloys*, 2nd ed. (Pergamon, New York, 1975).
[36] A. Kolmogorov, *Izvestia Akademia Nauk SSSR*, Series Mathematica Vol. 1 (Academic Science Bulletin USSR, 1937), p. 355.
[37] W. Johnson and R. Mehl, Trans. Am. Inst. Miner. (Metall.) Eng. **135**, 416 (1939).
[38] M. Avrami, J. Chem. Phys. **7**, 1103 (1939).
[39] P. Bruna, D. Crespo, R. Gonzalez-Cinca, and E. Pineda, J. Appl. Phys. **100**, 054907 (2006).
[40] T. Kruger, B. Merkau, W. Grosshans, and W. Holzapfel, High Press. Res. **2**, 193 (1990).
[41] N. V. C. Shekar and G. Rajan, Bull. Mater. Sci. **24**, 1 (2001).
[42] N. Sun, X. Liu, and K. Lu, Scr. Mater. **34**, 1201 (1996).
[43] J. Lopes-da-Silva and J. Coutinho, Energy Fuels **21**, 3612 (2007).
[44] M. Talukdar and P. Achary, Int. J. Recent Res. Appl. Phys. **3**, 92 (2010).
[45] C. Pistorius, E. Rapoport, and J. Clark, J. Chem. Phys. **48**, 5509 (1968).

[46] M. Frank, H. Scott, E. Aarestad, and V. Prakapenka, Geochim. Cosmochim. Acta **174**, 156 (2016).
[47] L. Senft and S. Stewart, J. Geophys. Res. **112**, E11002 (2007).
[48] R. S. McWilliams, J. H. Eggert, D. G. Hicks, D. K. Bradley, P. M. Celliers, D. K. Spaulding, T. R. Boehly, G. W. Collins, and R. Jeanloz, Phys. Rev. B **81**, 014111 (2010).
[49] H. Philipp, M. Hromalik, M. Tate, L. Koerner, and S. Gruner, Nucl. Instrum. Methods Phys. Res., Sect. A **649**, 67 (2011).
[50] B. H. Toby, J. Appl. Crystallogr. **34**, 210 (2001).